

Dalton Transactions

An international journal of inorganic chemistry

Accepted Manuscript

This article can be cited before page numbers have been issued, to do this please use: M. Alberti, G. Rossi, D. Boucherabine, F. Cargnoni, M. I. Trioni, G. Taini, D. Zakutna, A. Gentilin, L. orevi, A. Sartorel and A. Caselli, *Dalton Trans.*, 2026, DOI: 10.1039/D5DT02534F.



This is an Accepted Manuscript, which has been through the Royal Society of Chemistry peer review process and has been accepted for publication.

Accepted Manuscripts are published online shortly after acceptance, before technical editing, formatting and proof reading. Using this free service, authors can make their results available to the community, in citable form, before we publish the edited article. We will replace this Accepted Manuscript with the edited and formatted Advance Article as soon as it is available.

You can find more information about Accepted Manuscripts in the [Information for Authors](#).

Please note that technical editing may introduce minor changes to the text and/or graphics, which may alter content. The journal's standard [Terms & Conditions](#) and the [Ethical guidelines](#) still apply. In no event shall the Royal Society of Chemistry be held responsible for any errors or omissions in this Accepted Manuscript or any consequences arising from the use of any information it contains.

Photoactive Fe(III)pyclen complexes for light-driven aerobic oxidation of *p*-xylene

Received 00th January 20xx,
Accepted 00th January 20xx

DOI: 10.1039/x0xx00000x

Matteo Alberti,^a Greta Rossi,^b Djihed Boucherabine,^a Fausto Cargnoni,^{c,*} Mario Italo Trioni,^c Giulia Taini,^a Dominika Zakutna,^d Arianna Gentilin,^b Luka Đorđević,^b Andrea Sartorel^{b,*} and Alessandro Caselli^{a,c,*}

Iron complexes have drawn attention for decades as biomimetic models of enzyme active sites that promote oxidative transformations. Many reports indeed deal with catalytic systems where iron complexes catalyze the oxidation of organic compounds, exploiting chemical oxidants, including dioxygen, through thermal activation. Conversely, reports where the photochemical activation of iron complexes is proven are less frequent. In this work, we describe the photochemical activation of iron(III) pyclen complexes, [Fe(III)(X)2pyclen]X (pyclen = 3,6,9-triaza-1(2,6)-pyridinacyclodecapane; X = Cl, Br, OTf, **1a-c**; OTf = triflate, CF₃SO₃⁻), and their application to the aerobic oxidation of *p*-xylene with visible light (up to 415 nm). Complexes **1a-c** have been synthesized and characterized, combining structural analysis, Mössbauer spectroscopy, and magnetization. Notably, spectroscopic UV-Vis analyses combined with DFT and TD-DFT calculations show that they have an extended absorption up to the visible region attributed to (pyclen/X) ligand-to-metal transitions, and that the absorption of light may induce a homolytic cleavage of the Fe–X bond. The nature of X impacts the photochemical activity of the iron complexes towards the oxidation of *p*-xylene with visible light, with **1b** (X = Br) leading to the privileged formation of *p*-tolualdehyde, while **1a** (X = Cl) and **1c** (X = OTf) are almost inactive. The reactivity of **1b** is rationalized by the photochemical generation of bromine radical (Br•) as the active species operating through a hydrogen atom transfer (HAT) reactivity towards *p*-xylene, as supported by the Bond Dissociation Free Energy (BDFE) of H–Br (BDFE = 87 kcal/mol) and of the C–H bond in *p*-xylene (BDFE = 80 kcal/mol). Kinetic and EPR evidence support a radical autooxidation pathway. This work will guide new studies on the photochemical reactivity of iron complexes towards light-driven, sustainable organic oxidation processes.

Introduction

The selective oxidation of hydrocarbons plays a crucial role in industrial synthesis and academic research.¹ Despite recent efforts to use more sustainable routes, industrial oxidation processes heavily rely on highly toxic metal-oxo reagents (e.g., KMnO₄) and metal oxide surfaces.² Although progress in developing more sustainable processes has been reported in recent decades,³ the demand for selective, efficient, and eco-friendly oxidation methods continues to grow.

The use of iron⁴ - the most abundant transition metal on Earth - and its complexes has attracted considerable interest in oxidation catalysis for organic synthesis, biochemistry, and industrial applications.⁵ Significant advancements in this field over recent years have been highlighted in several comprehensive reviews.^{6–16} Natural mononuclear nonheme iron enzymes are pivotal in essential oxidative transformations, efficiently catalysing a wide range of

chemical reactions.^{17,18} Efforts to develop synthetic models that replicate Nature's strategies continue to be a highly active research area.^{19–25} In both these enzymes and their synthetic counterparts, high-valent iron-oxo intermediates, such as iron(III)-superoxo, iron(III)-peroxo, iron(III)-hydroperoxo, and iron(IV)- or iron(V)-oxo species, play a central role.^{17,26}

Iron(III)-superoxo species have been identified as active species in C–H bond activation and oxygen atom transfer (OAT) reactions.²⁷ However, their activity is largely limited to weak, activated C–H bonds in hydrocarbons. In contrast, the reactivity of nonheme iron(III)-hydroperoxo species remains a topic of debate and is the subject of extensive experimental and theoretical investigations.²⁸ Meanwhile, nonheme iron(IV)-oxo species are established as competent oxidants, capable of abstracting hydrogen atoms in C–H bond activation reactions.²³

Among nonheme catalysts, iron complexes with polyamine and aminopyridine ligands occupy a prominent position.^{29,30} Notably, iron(II) complexes of tetradentate N4 donor ligands, such as [Fe(CF₃SO₃)₂(pyclen-Me₃)], (pyclen = 3,6,9-triaza-1(2,6)-pyridinacyclodecapane; CF₃SO₃⁻ is the triflate anion further abbreviated OTf⁻), are readily oxidized by H₂O₂ to form a hydroperoxo iron(III) species.^{31,32} This species, following acid-triggered O–O bond cleavage, becomes active in the stereospecific hydroxylation of strong C–H bonds.³³

Our group has focused on the synthesis and coordination behavior of pyridine-based 12-membered tetraaza-macrocyclic ligands.^{34,35} We

^a Department of Chemistry, Università degli Studi di Milano, Via Golgi, 19, 20133 Milano, Italy. alessandro.caselli@unimi.it

^b Department of Chemical Sciences, University of Padova, via Marzolo 1, 35131 Padova, Italy. andrea.sartorel@unipd.it

^c Istituto di Scienze e Tecnologie Chimiche "G.Natta" CNR-SCITEC, via Golgi 19, 20133 Milano, Italy. fausto.cargnoni@scitec.cnr.it

^d Department of Inorganic Chemistry, Charles University, Hlavova 2030/8, 128 40, Prague 2, Czech Republic.

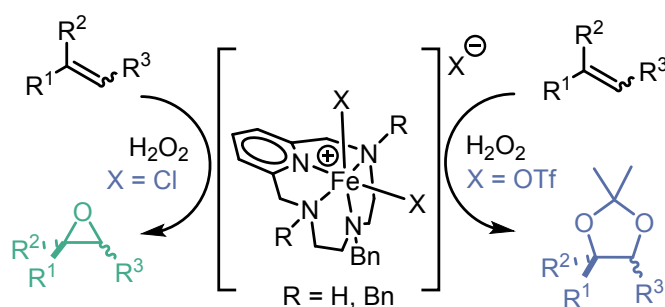
† Supplementary Information available: Supplementary data associated with this article, including Synthetic procedures, Macroscopic magnetization measurements, DFT calculations, Single crystal X-Ray diffraction analyses, Spectroscopic characterization, and catalytic tests, can be found in the Supplementary Information.



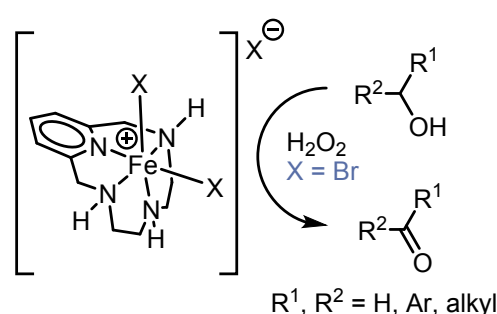
described the synthesis and characterization of robust $[\text{Fe(III)}\text{X}_2(\text{pyclen})]^+$ complexes, which are highly active and selective for alkene oxidation using hydrogen peroxide as the terminal oxidant, without the need for additives (Figure 1a).³⁶ Noteworthy, depending on the anion (X^-) of the iron(III) complex used as the catalyst, we observed selective formation of epoxide ($\text{X} = \text{Cl}$) or a clean dihydroxylation reaction ($\text{X} = \text{OTf}$). Intrigued by these results, we further explored the reactivity of iron(III) pyclen complexes in the selective oxidation of alcohols using H_2O_2 , without any acid co-catalyst (Figure 1b).³⁷ Hydrogen peroxide is an appealing oxidant since the only by-product is water; however, the ideal oxidant is surely molecular oxygen, O_2 , which can address sustainability priorities in industry.³⁸ In this context, the combined use of visible light and dioxygen for the photocatalytic oxidation of hydrocarbons offers an atom-economic and greener alternative to traditional methods.^{39,40}

While iron complexes have been extensively investigated in the chemical activation of oxidants, their reactivity with light towards photocatalytic processes remains less explored.⁴¹ These retain particular interest since the recent renaissance of photocatalysis towards sustainable processes and synthetic organic chemistry, with solar reforming being indeed an emerging technology for circular chemical industries.⁴² Recent examples dealt with FeX_3 ($\text{X} = \text{Cl}, \text{Br}$)

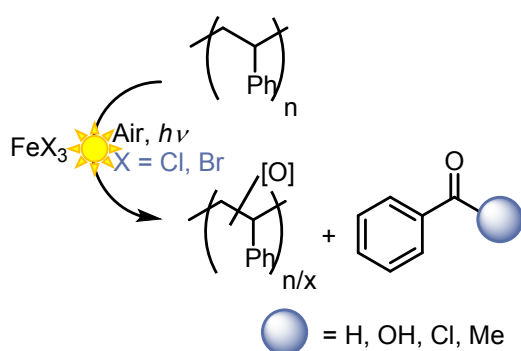
a) Tseberlidis, 2019



b) Panza, 2020



c) Oh, Stache, 2022-2023



d) This work

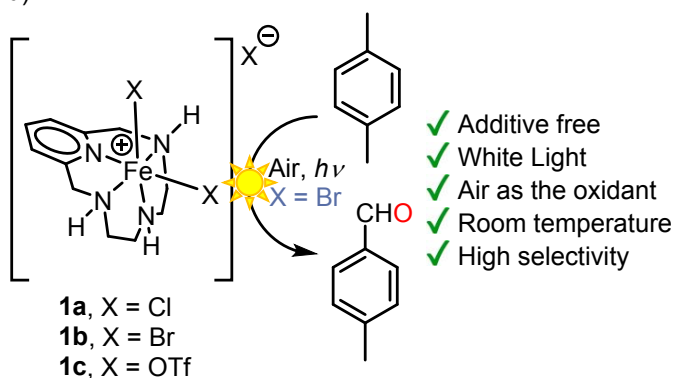


Figure 1. a-b) Oxidation reactions catalysed by $[\text{Fe(III)}\text{X}_2(\text{pyclen})]^+$ complexes using H_2O_2 as the terminal oxidant; c) photochemical valorisation of polystyrene with FeX_3 ($\text{X} = \text{Cl}, \text{Br}$); d) selective light-induced (white light or 405 nm LED) aerobic oxidation of *p*-xylene reported in this work.



Results and Discussion

Synthesis and characterization of Fe(III) Pycen complexes

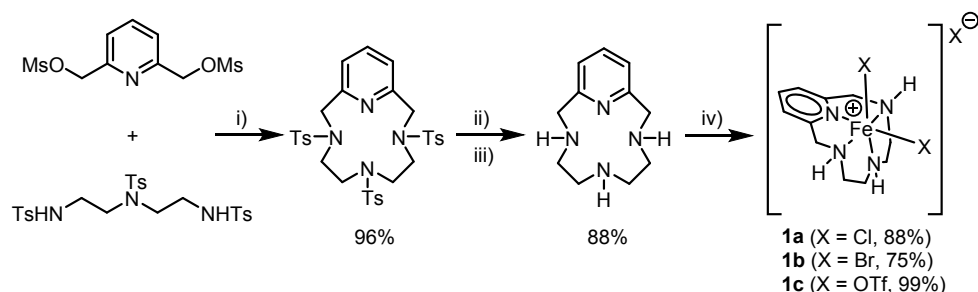
Complexes **1a-c** were obtained by treating pycen with the appropriate iron(III) salt precursor (Scheme 1). In the case of complexes **1a** and **1b**, they were recovered from the reaction medium as precipitates in high yield and purity. Conversely, the higher solubility of the triflate complex, **1c**, rendered its collection more complicated, and any attempt to precipitate the complex from acetonitrile met with failure. The product was then collected by evaporation of the solvent as a deep yellow oil in quantitative yield and then treated with cold diethyl ether to obtain a brownish precipitate. Nonetheless, HR-MS analysis confirmed the expected formation of the complex.

Several crystal structures of $[\text{FeX}_2(\text{pycen})]^+$ cationic complexes, balanced with various counterions, have been reported.^{37,46–50} Interestingly, crystallization of compound **1a** via solvent diffusion (methanol/diethyl ether, $v/v = 1:2$) led to the concomitant precipitation of two distinct crystal morphologies: clear, yellow, regular blocks (**1a**) and elongated, dark brown plates (**1a'**). While structural analysis of the former matched previously published work by Green and co-workers (CCDC No 1578766),⁴⁹ featuring a chloride counterion, the latter displayed a novel structure, which was determined via X-ray diffraction (Figures S1–S4, Tables S1–S7 in Supplementary Information, including a detailed comparison of the X-ray structural features of compounds **1a'** with analogous structures published in the Cambridge Crystallographic Data Centre, including **1a** and **1b**). X-ray diffraction analysis of **1a'** revealed that, although it shares the same molecular geometry and *cis*-folded tetraaza-macrocyclic configuration as **1a**, it incorporates a divalent $[\text{Fe}(\text{II})\text{Cl}_4]^{2-}$ anion in its second coordination sphere. The presence of $[\text{MCl}_4]^{n-}$ species as counterions in analogous cationic coordination compounds has been previously observed by our group³⁶ and others.^{49,51} Auto reduction of Fe(III) to Fe(II) accompanied by oxidation of the halide with concomitant release of X_2 gas has been previously reported.⁵²

In all these structures, the Fe(III) center adopts a distorted octahedral geometry, coordinated by the four nitrogen atoms of the macrocycle and two monodentate X-type ligands. The pycen scaffold displays a *cis*-folded conformation, which has been demonstrated by molecular mechanics calculations to be preferred when M–N bond lengths are greater than 2.0 Å.⁵³

We gained further insight into the structural distortion of these complexes with respect to an ideal octahedral arrangement by comparing experimental structures with those computed for the gas phase and solvated states of **1a** and **1b**. Interestingly, the crystalline structures are in better agreement with data extracted from solvated complexes than from gas-phase ones, as detailed in Tables S4 and S11 of the Supplementary Information section. Indeed, for both **1a** and **1b**, the relevant geometrical parameters of gas-phase molecules differ from the experimental crystalline values by almost 0.05 to 0.1 Å, while the inclusion of solvation effects in the computations reduces these discrepancies by more than half. This outcome suggests that the dissolution of **1a**, **1b**, and **1c** in a solvent with medium polarity partially mimics crystal field effects. This analysis, though limited to geometrical features, supports a proper description of the systems under investigation by the employed computational approach.

To elucidate the oxidation state of the iron complexes, Mössbauer spectroscopy was performed on solid-state samples at room temperature using nitrogen-flushed sample holders. Fitting results are summarized in Table S8, with a qualitative analysis provided in the Supplementary Information. As expected, complex **1a** exhibits high-spin Fe^{3+} center (see Figure S5, left). In contrast, complexes **1b** and **1c** display signatures of Fe^{2+} . For **1b**, this likely arises from partial reduction of FeBr_3 to FeBr_2 under vacuum and heating conditions (Figure S5, right). In the case of **1c**, however, the Fe^{2+} signal originates from impurities in the commercial $\text{Fe}(\text{OTf})_3$ precursor, which Mössbauer analysis revealed to contain up to 46% Fe^{2+} (Table S9). To resolve this, we synthesized in-house pure $\text{Fe}(\text{OTf})_3$ starting from pure anhydrous FeCl_3 , and when complex **1c** was prepared with this iron(III) triflate source, the Mössbauer spectroscopy did not show any evident sign of the presence of Fe^{2+} (Figure S6, right).



Scheme 1. Synthetic route used to obtain ferric complexes **1a-c**. i) K_2CO_3 , CH_3CN , reflux; ii) H_2SO_4 conc., microwave; iii) NaOH ; iv) FeX_3 , CH_3CN , Δ . Commercially available iron(III) trifluoromethanesulfonate may be heavily contaminated with the iron(II) species (up to 43%, see *Supplementary Information* and Table S9). Therefore, we synthesized an $\text{Fe}(\text{III})(\text{OTf})_3$ precursor in-house from ferric chloride to avoid any trace of $\text{Fe}(\text{II})$, as detailed in the *Supplementary Information*.



The spin states of complexes **1a** and **1b** were further assessed using macroscopic magnetization measurements. Zero Field Cooled (ZFC) and Field Cooled (FC) magnetization curves were measured at 0.5 T, and in both samples, they overlapped completely. The temperature dependence of the molar magnetic susceptibility-temperature product ($\chi_M T$) for complexes **1a** and **1b** is presented in Figure 2. For complex **1a** (Figure 2a), deviation from ideal Curie or Curie-Weiss (represented by the teal dashed line in Figure 2a) behavior at low and high temperatures indicates antiferromagnetic interactions and zero-field splitting. These effects were modelled using the modified Van Vleck approach.⁵⁴ The result, which incorporates both zero-field splitting and axial distortion, yielded an excellent fit (Figure 2a, magenta line). The fit parameters are summarized in Table 1, while the equation, derived for this system, is as follows:

$$\chi = \frac{\chi_z + 2\chi_x}{3}$$

$$\chi_z = \frac{Ng_z^2\mu_B^2}{4k(T-\theta)} \cdot \frac{1 + 9e^{-\frac{2D}{k(T-\theta)}} + 25e^{-\frac{6D}{k(T-\theta)}}}{1 + e^{-\frac{2D}{k(T-\theta)}} + e^{-\frac{6D}{k(T-\theta)}}}$$

$$\chi_x = \frac{Ng_x^2\mu_B^2}{4} \cdot \frac{\frac{9}{k(T-\theta)} + \frac{8}{D} - \frac{11e^{-\frac{2D}{k(T-\theta)}}}{2D} - \frac{5e^{-\frac{6D}{k(T-\theta)}}}{2D}}{1 + e^{-\frac{2D}{k(T-\theta)}} + e^{-\frac{6D}{k(T-\theta)}}}$$

In contrast, complex **1b** displays typical antiferromagnetic behavior with a gradual decline in $\chi_M T$ at low temperatures (Figure 2b). The Curie-Weiss law describes its magnetic profile well across the full temperature range, consistent with a high-spin Fe³⁺ center. The effective magnetic moment of 5.87(4) μ_B closely matches the spin-only value of 5.91 μ_B , with a Curie-Weiss temperature of -7.66 K (Table 2).

These data nicely agree with theoretical computations on gas-phase anions derived from **1a**, **1b**, and **1c**. Indeed, the wavefunction analysis indicates that in all systems the oxidation state of iron is +3, and the most stable spin arrangement presents 5 unpaired electrons in the half-filled *d* shell of the metal atom. The oxidation state of the metal atom remains +3 also considering medium- and low-spin arrangements, where the number of unpaired electrons is 3 and 1, respectively. As for the energetics, medium- and low-spin states are less stable than the high-spin arrangement by more than 10 kcal/mol in all compounds, and solvation in acetonitrile does not alter this picture (data are collected in Table S10). It is therefore unlikely that thermal energy at 298 K and solvation might induce spin flips or changes in the oxidation state of iron. Based on Mössbauer spectroscopy, macroscopic magnetic measurements, and ab initio computations, we can assess that - at the experimental conditions considered in this study - **1a**, **1b**, and **1c** contain a Fe(III) atom with 5 unpaired electrons.

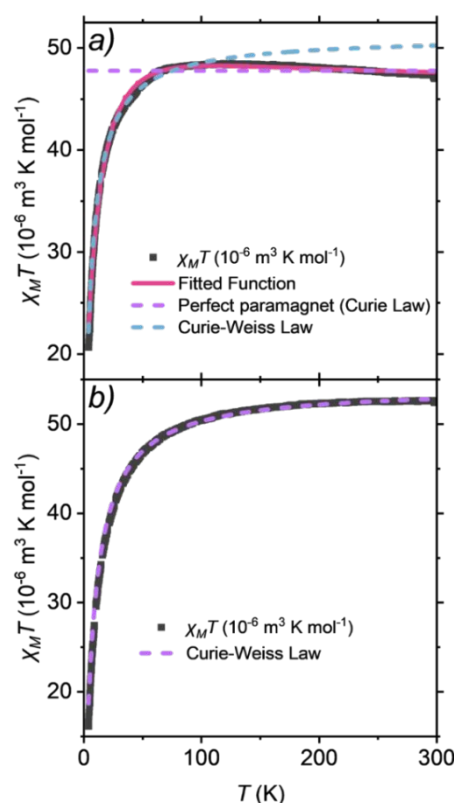


Figure 2. $\chi_M T$ product as a function of temperature, for compound **1a** (a) and compound **1b** (b).

Table 1. Fitted parameters for $\chi_M T$ product of compound **1a**.

Parameter	Value
g_{tot}^a	2.041(2)
D	20.0(1) cm^{-1}
ϑ	-2.44(4) K

$$^a g_{tot} = (2g_x + g_z)/3$$

Table 2. Results from Curie law and Curie - Weiss law fits for compounds **1a** and **1b**.

Sample	μ_{eff} (μ_B , Curie)	μ_{eff} (μ_B , Curie - Weiss)	ϑ_{CW} (K)
1a	5.5164(4)	5.7063(7)	-5.28
1b	5.7506(2)	5.87(4)	-7.66



Spectroscopic characterization of the complexes

Figure 3 reports the experimental and calculated UV-Vis spectra of **1a**, **1b**, and **1c** in acetonitrile; the calculated spectra represent the experimental profile well, except that computed absorptions fall at somewhat different energies with respect to experimental ones, which comes as no surprise considering the limitations of the TD-DFT scheme.⁵⁵ Quite importantly, in the specific systems studied here, the difference between computed and measured spectra allows for a direct comparison between absorption peaks.

The experimental spectrum of **1a** reveals the presence of three main absorption bands centered at 258, 320, and 377 nm. These features are also found in the simulated spectra. As expected, none of the three peaks comes from a single absorption transition. On the contrary, they should be ascribed to three clusters of pycnen/Cl ligand-to-metal electronic transitions, which become less intense and more dispersed as the photon energy decreases (see Supplementary Information). The inspection of these data revealed the presence of chlorine-to-iron transitions, and the corresponding photon energy resides in the range relevant to the experiments presented here. This prompted us to computationally investigate the possibility of Fe–Cl homolytic bond dissociation. The computed threshold for homolytic breaking of a Fe–Cl bond is 3.34 eV (corresponding to a wavelength of 371 nm, thus falling within the lowest energetic absorption band (green bands in Figure 3a-b). As can be seen in Figure 4 (left panel), the wavefunction analysis of the transitions just above the threshold reveals that, upon excitation, a single electron is transferred from the chloride ligands to the metal center, and the complex gains enough energy to expel a chlorine radical. Though this is not a rigorous proof that homolytic dissociation occurs, since it does not consider alternative relaxation phenomena and other limiting effects, it is a significant indication that this might be the case, being the excited moiety higher in energy than the species corresponding to homolytic dissociation.

In **1b**, the less energetic absorption bands are redshifted with respect to **1a**, and they are centered at 395 and 470 nm, respectively (see Figure 3c). Besides the extension of the absorption towards longer wavelengths, the attribution of the electronic transitions follows similar considerations to what was discussed previously for **1a**. The computed threshold for homolytic dissociation of Fe–Br bond in **1b** is 2.94 eV (corresponding to 421 nm) and falls between the less energetic electronic transitions (green and orange bands in Figure 3c-d). In particular, the calculated band centered at 382 nm (green band in Figure 3d) presents a neat Br-to-metal charge transfer, as shown in Figure 4 (middle). This intense transition is likely to be the main reason for photoinduced homolytic dissociation of a Fe–Br bond in **1b** (*vide infra*).

The experimental spectrum of **1c** is somewhat different from **1a** and **1b** ones. Indeed, it presents two intense bands centered at 249 and 326 nm, followed by a low-intense broad band centered at 379 nm. The recorded data evidence the presence of another smooth and broad shoulder in the absorbance, located at even longer

wavelengths. This feature suggests that several transitions with low intensity are widely distributed around 500 nm. The theoretical simulation of **1c**, indeed, produced two neat peaks at 248 and 354 nm, in agreement with the recorded data. However, their intensities are comparable to each other, while experimentally the peak at 249 nm is much more intense than the one at 326 nm. At longer wavelengths, first principles computations predict a sparse set of transitions, distributed from 550 to 650 nm. This is consistent with the experiment, even if the recorded data are not strictly reproduced by theory. Overall, we can affirm that the allowed electronic transitions of **1c** cover a wider energy range as compared to **1a** and **1b**. Most of them have partial ligand-to-metal charge transfer character, and they are almost comparable in intensity to one another, thus generating a poorly structured spectrum. Likely, the difficulty in reproducing the fine details of the experimental spectrum of **1c** reflects the more complex electronic structure of this moiety with respect to **1a** and **1b**, consistently with the reliability of the computational approach adopted.⁵⁶ We also note that the predicted geometry of **1c** could not be confirmed by experimental data, at variance with respect to **1a** and **1b**.

Direct calculation of the energy required to promote the homolytic cleavage of Fe–OTf bond in **1c** was hampered by a proper description of the OTf• radical by DFT (see Supplementary information). We thus estimated a value of 3.89 eV (corresponding to a wavelength of 319 nm), by comparing the relative stability of Cl• and OTf• radicals with the CISD method in terms of the BDFE of H–Cl and H–OTf (CISD stands for Configuration Interaction with Singles and Doubles electron excitations). This high value is in line with the expected instability of the oxygen-centered OTf• radical and rules out the possibility of generating it from **1c** with visible light.



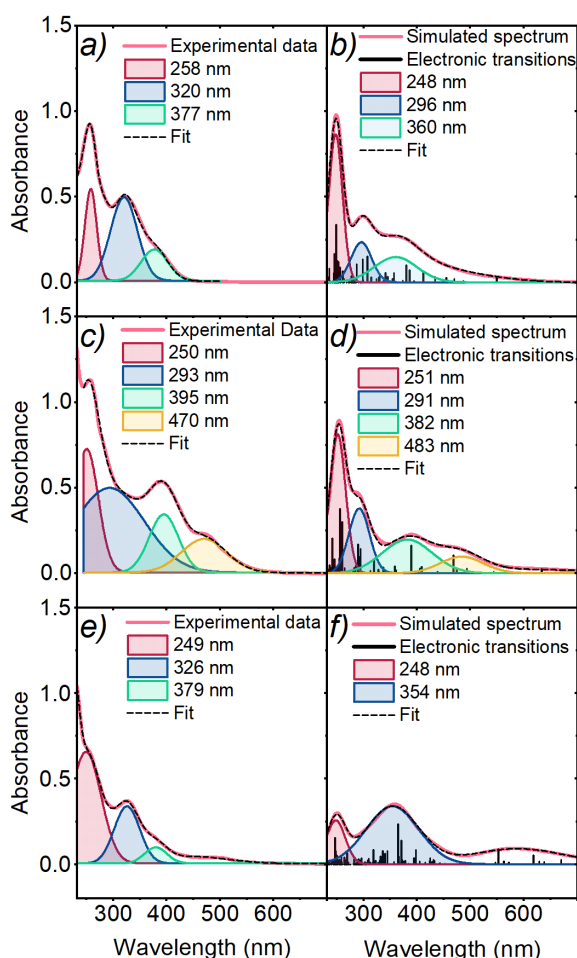


Figure 3. UV-Vis experimental (left) and theoretical (right) spectra for **1a** (top) (a and b, respectively), **1b** (middle) (c and d), and **1c** (bottom) (e and f) complexes. Left panels: the experimental data are reported as a solid red line, while data obtained by Gaussian fitting are depicted as a dashed black line. Right panels: the computed electronic transitions are reported as solid black lines; the solid red line (the simulated spectrum) is obtained by smearing delta-like absorption peaks with a Gaussian function, and the dashed black line is obtained by fitting the simulated spectrum with the same criterion adopted for experimental data. The fitting Gaussian functions embrace several transitions each, and they are reported as a guide for the eye. In Figure S10 (Supplementary Information), all the Gaussians that were used to fit the spectra are reported.

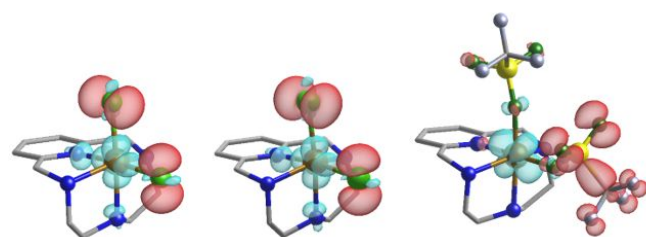


Figure 4. Representative electron density maps for sample electronic transitions above the dissociation threshold of **1a** (left), **1b** (middle), and **1c** (right). Maps are obtained as the difference between the electron density of the excited state and the ground state, and they refer to the main components of transitions at 357 nm (left), 389 nm (middle), and 486 nm (right). Positive values are in light-blue, negative values in red. In the three transitions reported, electron excitation removes an electron from the ligands (X) and localizes it onto the Fe atom, which is likely to induce homolytic Fe–X dissociation when this is energetically allowed, i.e. in the case of **1a** and **1b**.

Photochemical aerobic oxidation of *p*-xylene

View Article Online

DOI: 10.1039/D5DT02534F

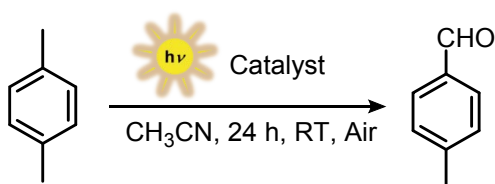
With the indication from UV-Vis spectroscopy and DFT calculations on the possibility of promoting the homolytic cleavage of the Fe–X bond by light, we finally explored the photochemical activity of iron pycen complexes towards the light driven aerobic oxidation of organic substrates, in particular of *p*-xylene. Among its oxidation products is terephthalic acid, a chemical of interest for polymer industry with an annual production of ca 90 million tons in 2024 through the Amoco process, employing a cobalt-manganese-bromide catalyst in acetic acid as the solvent, at 175–225°C temperature and 15–30 bar air pressure.^{57–60} Besides terephthalic acid, intermediate oxidation products retain interest, such as *p*-methylbenzyl alcohol, *p*-tolualdehyde, and *p*-toluic acid. The oxidation of *p*-xylene requires the activation of the benzylic C–H bonds, characterized by a Bond Dissociation Free Energy of 80 kcal/mol; the oxidative activation of C–H bonds is a very hot topic,^{61–66} and there is current interest in developing systems for the photochemical oxidation of *p*-xylene exploiting visible light.

Recently, Sun and co-workers used UV irradiation (Hg lamp, 500W, 0–2 Sun) to boost an ozonization process, reaching 84% terephthalic yield in acetonitrile solvent.⁶⁷ The tetrabutylammonium decatungstate photocatalyst was employed in a continuous-flow photoreactor achieving >90% yield of terephthalic acid upon irradiation at 365 nm.⁶⁸ The same irradiation wavelength was exploited to activate titanium oxide nanoparticles, for the oxidation of *p*-xylene to *p*-methylbenzyl alcohol and *p*-tolualdehyde as the primary oxidation products.⁶⁹ In alternative, quinone organic photocatalysts, able to promote photochemical hydrogen atom abstraction (hydrogen atom transfer – HAT – reactivity), were considered for the oxidation of *p*-xylene with visible light in acetone solvent, obtaining *p*-toluic acid as the main product, while terephthalic acid was obtained in ca 27% yield from overoxidation of *p*-toluic acid.⁷⁰

As anticipated in the introduction, inspired by the recent reports by Oh and Stache dealing with the photochemical generation of halogen radicals from FeX₃ for the photooxidation of commercial polystyrene,⁴³ we envisioned to investigate the photochemical activity of iron pycen derivatives. The excitation of ligand-to-metal charge transfer bands in coordination complexes is indeed a convenient strategy for photochemical generation of halogen radicals using low-energy light.⁷¹ Halogen radicals are reactive species for C–H activation⁷² since they can induce HAT reactivity;^{73,74} the key reactivity descriptor is the bond dissociation energy of the H–Halogen bond, being 102 kcal/mol for HCl (identifying Cl• as a potent hydrogen atom abstractor), 87 kcal/mol for HBr and 71 kcal/mol for HI (I• is indeed not useful for HAT).⁷⁵



Table 3. Photocatalytic oxidation of *p*-xylene to *p*-tolualdehyde. Standard conditions: 1 ml of solution containing 80 mM *p*-xylene and 2.5 mM iron catalyst in acetonitrile, irradiation with white light (33 mWcm⁻²) for 24 h under air atmosphere. a: irradiation with blue LED (405 nm, 18 mWcm⁻²) for 2 hours.



#	Catalyst	Deviations from standard conditions	<i>p</i> -tolualdehyde yield(%) / selectivity(%)	Other products, yield (%)
1	1a	-	≈ 1	-
2	1b	-	31±5 / 79±5	<i>p</i> -toluic acid 7.5±3 terephthalic acid 1.5±0.5 <i>p</i> -methylbenzyl alcohol < 1
3	1c	-	5	-
4	1b	O ₂ instead of air	31 / 81	<i>p</i> -toluic acid 6 <i>p</i> -methylbenzyl alcohol 1
5	1b	Acetone as the solvent	20 / 55	<i>p</i> -toluic acid 15 <i>p</i> -methylbenzyl alcohol < 1
6	1b	Propylene carbonate as the solvent	2 / >95	-
7	1b	In <i>p</i> -xylene neat	-	-
8	FeCl ₃	-	24±3 / 56	<i>p</i> -toluic acid 13 terephthalic acid 1 <i>p</i> -methylbenzyl alcohol 5
9	FeBr ₃	-	20 / 66	<i>p</i> -toluic acid 6 <i>p</i> -methylbenzyl alcohol 4
10	FeCl ₃	Acetone as the solvent	4 / 22	<i>p</i> -toluic acid 5 terephthalic acid 9
11	1b	LED 405 nm ^a	21 / 87	<i>p</i> -toluic acid 1 <i>p</i> -methylbenzyl alcohol 2

We thus tested the photochemical reactivity of **1a-c** towards the oxidation of *p*-xylene (80 mM in acetonitrile solution), using a home-made photoreactor exploiting cheap household lamps emitting white light (33 mW/cm², equivalent to 1/3 of the irradiation by the sun),⁷⁶ see the emission spectrum in Figure S11 overlapped with absorption spectra of Fe pyclen derivatives. The reaction mixtures from the photocatalytic tests were analyzed through ¹H-NMR, adding mesitylene as the internal standard (Figure S12). The results are summarized in Table 3. The results can be discussed as follows:

(a) **1b** was the only iron complex being significantly active (entries 1-3 in Table 3), promoting the formation of *p*-tolualdehyde as the main reaction product (31±5% yield, corresponding to 9.9±1.6 turnovers based on the iron catalyst, entry 2 in Table 3). The results were obtained from 6 replicated experiments, including two different batches of **1b**. Control experiments confirmed that light, the iron

catalyst, and the aerobic atmosphere are necessary for the photochemical oxidation of *p*-xylene. Running the reaction under O₂ atmosphere did not lead to a significant improvement of the yield and selectivity (entry 4 in Table 3).

(b) The selectivity for *p*-tolualdehyde among other oxidation products was 79±5%, with *p*-toluic acid being also detected. The C-H bond in aromatic aldehydes are stronger than the C-H bond of a benzylic -CH₃ group (the C-H bond in benzaldehyde has a BDFE of 89 kcal/mol, while the C-H bond in *p*-xylene has a BDFE of 80 kcal/mol);^{63,75} overoxidation of *p*-tolualdehyde is thus more demanding than oxidation of *p*-xylene, and explains the good selectivity of the process.

(c) The reactivity of **1b** is maintained also in acetone as the solvent,⁴³ entry 5 in Table 3, although with a decreased selectivity (*p*-tolualdehyde yield 20%, selectivity 55%); we also tested the



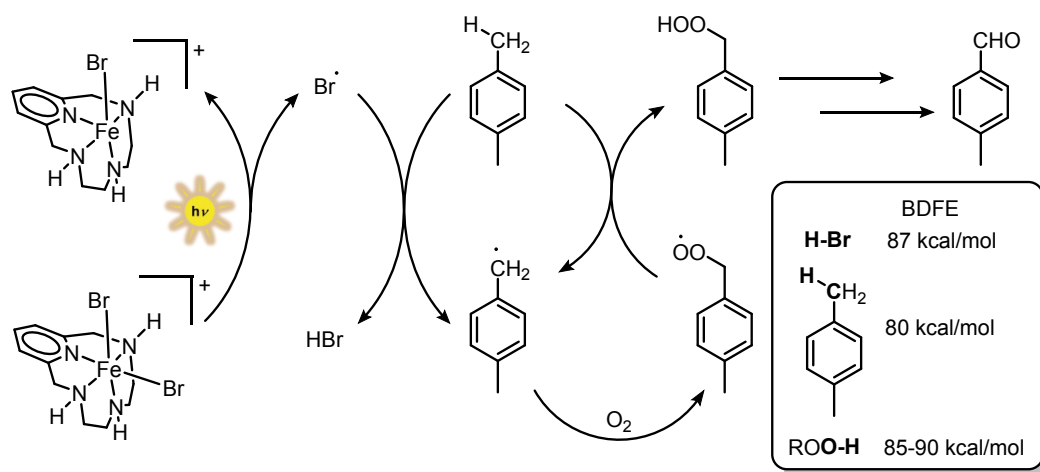
possibility of conducting the reaction in propylene carbonate as a green solvent, where a decreased yield of 2% was registered (entry 6 in Table 3); no reactivity was observed in neat *p*-xylene (entry 7 in Table 3). These results suggest a non-innocent role of the solvent in promoting the target reactivity.

(d) A photochemical reactivity was observed also with FeCl_3 and with FeBr_3 ,⁴³ although with slightly lower yield with respect to **1b** (entries 8-10 in Table 3). In particular, we observed a decrease in the reaction selectivity and the increased formation of *p*-methylbenzyl alcohol along with *p*-toluic acid as major by-products.

(e) The reaction with **1b** was accomplished by using monochromatic LED at 405 nm as light source, leading to 21% yield of *p*-tolualdehyde after 2 h (selectivity 87%, entry 11 in Table 3). Estimation of the absorbed photons with a power meter enabled to determine a quantum yield ϕ_{405} for the production of *p*-tolualdehyde of 0.14%. All indications above suggest the photoinduced generation of bromine radical participating in a HAT reactivity towards *p*-xylene, forming H-Br and the *p*-xylene radical; this will react with dioxygen to form an organic peroxy free radical that can engage HAT reactivity with *p*-xylene and feed a chain process (Scheme 2). An EPR analysis in the presence of 5-*tert*-butoxycarbonyl 5-methyl-1-pyrrolidine N-oxide (BMPO) spin trap⁷⁷ revealed the appearance of a multi-component signal compatible with an adduct between BMPO and peroxides as reactive oxygen species,^{78,79} although the low intensity

of the signal did not allow a reasonable simulation and identification of the components (Figure S13; BMPO was preferred to DMPO 2,5,5-dimethyl-1-pyrrolidine-N-oxide – due to its higher stability;^{77,78} indeed, very weak EPR signals were observed under the same conditions with DMPO spin trap). Organic hydroperoxides are characterized by BDFE of the O–H bond around 85-90 kcal/mol (i.e. BDFE referred to the $\text{ROO-H} / \text{ROO}\cdot$ couple).⁶³ The occurrence of a radical based process is also suggested by the kinetic profile of the reaction with **1b**, showing the expected initiation/propagation/termination phases (Figure S14).

Surprisingly, almost no reactivity was observed for **1a** under analogous conditions: in principle, photochemical homolysis of Fe–Cl in **1a** should lead to the formation of very reactive $\text{Cl}\cdot$. The poor reactivity of **1a** may be ascribed to a fast deactivation of the excited state and is currently under further investigation. On the other hand, the high energetic requirement for homolytic bond cleavage of Fe–OTf in **1c** is responsible for the low activity of this complex. We finally verified the stability of the active Fe pycen complex **1b** under photocatalysis conditions, where UV-Vis analysis revealed minor changes of the absorption spectrum of the compound, suggesting the stability of the Fe(III)pycen motif (Figure S15). For comparison, a major bleaching of the absorption bands are instead observed for FeBr_3 (Figure S15).



Scheme 2. Proposed photochemical mechanism and competent BDFE values.

Conclusions

In this work, we have reported the synthesis, characterization and photocatalytic reactivity of iron(III) complexes with tetradentate *N*4 3,6,9-triaza-1(2,6)-pyridinacyclodecaphane ligand (pycen), $[\text{Fe}(\text{III})(\text{pycen})\text{X}_2]\text{X}$ ($\text{X} = \text{Cl}$, **1a**; $\text{X} = \text{Br}$, **1b**; $\text{X} = \text{OTf}$, **1c**). In particular, the nature of the counterion has a marked effect on the photocatalytic reactivity of the complexes, enabling the challenging and ambitious light driven aerobic oxidation of *p*-xylene.

The crystal structure of **1a** shows an octahedral Fe(III) center with a cis-folded pycen configuration, with two chloride anions completing

the iron coordination sphere, consistently with **1b** and **1c**. Mössbauer and macroscopic magnetic measurements confirmed that the spin state in all the complexes is 5/2, which is consistent with the results that DFT calculations disclosed. The photochemical reactivity of the title complexes was envisaged based on the absorption features in solution, extending up to the visible region and associated to (pycen/X) ligand-to-iron transitions based on TD-DFT calculations. These absorption features were successfully exploited for the photochemical generation of bromine radicals ($\text{Br}\cdot$) from **1b**, responsible for the aerobic oxidation of *p*-xylene to *p*-tolualdehyde under visible light (up to 9.9 ± 1.6 turnovers for the Fe complex, with



a *p*-tolualdehyde selectivity up to 79±5% among other oxidation products, and a quantum yield of 0.14% at 405 nm).

We believe that this work will contribute to the design of novel photochemical routes exploiting coordination complexes of earth-abundant transition metals; besides oxidation of substrates of industrial interest like *p*-xylene considered in this work, applications in the photochemical valorization of plastics are appearing in recent literature. Future directions in this field should consider the development of aqueous systems for the valorization of abundant raw materials such as glycerol or furfural derivatives, while possibly red-shifting the use of light towards the visible region.

Author contributions

Matteo Alberti: Investigation, Data curation, Writing - original draft, Visualization. Greta Rossi, Arianna Gentilin, Luka Đorđević: Investigation, Data curation. Djihed Boucherabine: Data curation. Formal Analysis. Fausto Cargnoni, Mario Italo Trioni: Methodology, Theoretical calculations. Giulia Taini: Structure determination by single crystal X-Ray Diffraction, Data curation. Dominika Zakutna: Writing - review & editing. Andrea Sartorel, Alessandro Caselli: Conceptualization, Methodology, Writing - review & editing, Supervision, Project administration, Funding acquisition.

Conflicts of interest

There are no conflicts to declare.

Data availability

The data supporting the article have been included as part of the Supplementary Information.

Acknowledgements

We thank the MUR-Italy (PRIN 2022, PROMETEO project-2022KPK8WM and FORCEFUL project-20224KN85Y), the University of Milan (PSR 2022 – financed project “Catalytic strategies for the synthesis of high added-value molecules from bio-based starting materials” and Ph.D. fellowships to M. A.), and the European Union – Next Generation UE (project “PHOTOCORE” P2022ZSPWF to A.S.) for financial support. Unitech – COSPECT (<https://www.cospect.it/>), Università degli Studi di Milano, is gratefully acknowledged for HR MS and XRD analyses. DZ acknowledges the assistance provided by the Advanced Multiscale Materials for Key Enabling Technologies project, supported by the Ministry of Education, Youth, and Sports of the Czech Republic Project No. CZ.02.01.01/00/22_008/0004558, Co-funded by the European Union. D.Z. was supported by Charles University Research Centre program No. UNCE/24/SCI/010.

Notes and references

- J. H. E. Teles, I. Ermans, G. Franz and R. A. Sheldon, in *Ullmann's Encyclopedia of Industrial Chemistry*, 2015, pp. 1–103.
- W. J. Mijs, C. R. H. I. De Jonge and Editors, *Organic Syntheses by Oxidation with Metal Compounds*, Plenum, 1986.
- J.-E. Bäckvall and Editor, *Modern Oxidation Methods, 2nd Completely Revised*, Wiley-VCH Verlag GmbH & Co. KGaA, 2010.
- A. Furstner, Iron Catalysis in Organic Synthesis: A Critical Assessment of What It Takes To Make This Base Metal a Multitasking Champion. *ACS Cent Sci*, 2016, **2**, 778–789.
- I. Bauer and H.-J. Knölker, *Chem. Rev.*, 2015, **115**, 3170–3387.
- R. J. M. K. Gebbink and M. E. Moret, *Non-Noble Metal Catalysis: Molecular Approaches and Reactions*, Wiley-VCH Verlag GmbH & Co, 2018.
- S. M. Hoelzl, P. J. Altmann, J. W. Kueck and F. E. Kuehn, *Coord. Chem. Rev.*, 2017, **352**, 517–536.
- I. Gamba, Z. Codola, J. Lloret-Fillol and M. Costas, *Coord. Chem. Rev.*, 2017, **334**, 2–24.
- K. Gopalaiah, *Chem. Rev.*, 2013, **113**, 3248–3296.
- T. Wai-Shan, G. Q. Chen, Y. Liu, C. Y. Zhou and C. M. Che, *Pure Appl. Chem.*, 2012, **84**, 1685–1704.
- E. P. Talsi and K. P. Bryliakov, *Coord. Chem. Rev.*, 2012, **256**, 1418–1434.
- M. Costas, *Coord. Chem. Rev.*, 2011, **255**, 2912–2932.
- S. Enthaler, K. Junge and M. Beller, *Angew. Chem., Int. Ed. Engl.*, 2008, **47**, 3317–3321.
- A. Correa, O. Garcia Mancheno and C. Bolm, *Chem. Soc. Rev.*, 2008, **37**, 1108–1117.
- W. Nam, *Acc. Chem. Res.*, 2007, **40**, 522–531.
- E. Rose, B. Andrioletti, S. Zrig and M. Quelquejeu-Etheve, *Chem. Soc. Rev.*, 2005, **34**, 573–583.
- M. Guo, T. Corona, K. Ray and W. Nam, *ACS Cent. Sci.*, 2019, **5**, 13–28.
- M. L. Neidig and E. I. Solomon, *Chem. Comm.*, 2005, 5843–5863.
- L. Vicens and M. Costas, *Dalton Trans.*, 2018, **47**, 1755–1763.
- O. Cusso, M. W. Giuliano, X. Ribas, S. J. Miller and M. Costas, *Chem. Sci.*, 2017, **8**, 3660–3667.
- G. Olivo, O. Cusso, M. Borrell and M. Costas, *J. Biol. Inorg. Chem.*, 2017, **22**, 425–452.
- G. Olivo, O. Cusso and M. Costas, *Chem. - Asian J.*, 2016, **11**, 3148–3158.
- W. Nam, Y. M. Lee and S. Fukuzumi, *Acc. Chem. Res.*, 2014, **47**, 1146–1154.
- J. Yoon, S. A. Wilson, Y. K. Jang, M. S. Seo, K. Nehru, B. Hedman, K. O. Hodgson, E. Bill, E. I. Solomon and W. Nam, *Angew. Chem., Int. Ed.*, 2009, **48**, 1257–1260.
- M. Costas, M. P. Mehn, M. P. Jensen and L. Que Jr., *Chem. Rev.*, 2004, **104**, 939–986.
- S. H. Bae, X.-X. Li, M. S. Seo, Y.-M. Lee, S. Fukuzumi and W. Nam, *J. Am. Chem. Soc.*, 2019, **141**, 7675–7679.



- 27 E. Tacchi, E. Anxolabéhère-Mallart, A. Aukauloo, C. Fave, M. Robert and A. Sartorel, *Angew. Chem. Novit*, 2025, **1**, e70007.
- 28 W. Nam, *Acc. Chem. Res.*, 2015, **48**, 2415–2423.
- 29 K. P. Bryliakov and E. P. Talsi, *Coord. Chem. Rev.*, 2014, **276**, 73–96.
- 30 C.-L. Sun, B.-J. Li and Z.-J. Shi, *Chem. Rev.*, 2011, **111**, 1293–1314.
- 31 J. Serrano-Plana, W. N. Oloo, L. Acosta-Rueda, K. K. Meier, B. Verdejo, E. García-España, M. G. Basallote, E. Münck, L. Que, A. Company and M. Costas, *J. Am. Chem. Soc.*, 2015, **137**, 15833–15842.
- 32 J. Serrano-Plana, A. Aguinaco, R. Belda, E. García-España, M. G. Basallote, A. Company and M. Costas, *Angew. Chem., Int. Ed.*, 2016, **55**, 6310–6314.
- 33 J. Serrano-Plana, F. Acuña-Parés, V. Dantignana, W. N. Oloo, E. Castillo, A. Draksharapu, C. J. Whiteoak, V. Martin-Diaconescu, M. G. Basallote, J. M. Luis, L. Que Jr., M. Costas and A. Company, *Chem. Eur. J.*, 2018, **24**, 5331–5340.
- 34 N. Panza, G. Tseberlidis, A. Caselli and R. Vicente, *Dalton Trans.*, 2022, **51**, 10635–10657.
- 35 G. Tseberlidis, D. Intrieri and A. Caselli, *Eur. J. Inorg. Chem.*, 2017, **2017**, 3589–3603.
- 36 G. Tseberlidis, L. Demonti, V. Pirovano, M. Scavini, S. Cappelli, S. Rizzato, R. Vicente and A. Caselli, *ChemCatChem*, 2019, **11**, 4907–4915.
- 37 N. Panza, A. di Biase, S. Rizzato, E. Gallo, G. Tseberlidis and A. Caselli, *Eur. J. Org. Chem.*, 2020, **2020**, 6635–6644.
- 38 A. N. Campbell and S. S. Stahl, *Acc. Chem. Res.*, 2012, **45**, 851–863.
- 39 S. Fukuzumi and K. Ohkubo, *Chem. Sci.*, 2013, **4**, 561–574.
- 40 S. Fukuzumi, *Dalton Tran.*, 2015, **44**, 6696–6705.
- 41 W. J. Zhou, X. D. Wu, M. Miao, Z. H. Wang, L. Chen, S. Y. Shan, G. M. Cao and D. G. Yu, *Chem. Eur. J.*, 2020, **26**, 15052–15064.
- 42 S. Bhattacharjee, S. Linley and E. Reisner, *Nat. Rev. Chem.*, 2024, **8**, 87–105.
- 43 S. Oh and E. E. Stache, *J. Am. Chem. Soc.*, 2022, **144**, 5745–5749.
- 44 S. Oh and E. E. Stache, *ACS Catal.*, 2023, **13**, 10968–10975.
- 45 X. Y. Yuan, C. C. Wang and B. Yu, *Chin. Chem. Lett.*, 2024, **35**, 109517.
- 46 N. W. Alcock, D. H. Busch and C. Y. Liu, *CSD Commun.*, *CCDC 639154*, DOI:10.5517/ccpg2w2.
- 47 M. A. Mekhail, K. Pota, T. M. Schwartz and K. N. Green, *RSC Adv.*, 2020, **10**, 31165–31170.
- 48 S. M. Brewer, P. M. Palacios, H. M. Johnston, B. S. Pierce and K. N. Green, *Inorg. Chim. Acta*, 2018, **478**, 139–147.
- 49 S. M. Brewer, K. R. Wilson, D. G. Jones, E. W. Reinheimer, S. J. Archibald, T. J. Prior, M. A. Ayala, A. L. Foster, T. J. Hubin and K. N. Green, *Inorg. Chem.*, 2018, **57**, 8890–8902.
- 50 S. M. Brewer, T. M. Schwartz, M. A. Mekhail, L. S. Turan, T. J. Prior, T. J. Hubin, B. G. Janesko and K. N. Green, *Organometallics*, 2021, **40**, 2467–2477.
- 51 N. W. Alcock, D. H. Busch and C. Y. Liu, *CSD Commun.*, *CCDC 639153*, DOI:10.5517/ccpg2v1.
- 52 A. Abedi, N. Safari, V. Amani and H. R. Khavasi, *Dalton Trans.*, 2011, **40**, 6877–6885. DOI: 10.1039/D5DT02534F
- 53 V. Felix, J. Costa, R. Delgado, M. G. B. Drew, M. T. Duarte and C. Resende, *J. Chem. Soc., Dalton Trans.*, 2001, 1462–1471.
- 54 O. Kahn, *Molecular magnetism*, VCH-Verlag, Weinheim, New York, 1993.
- 55 M. Cazzaniga, F. Cargnoni, M. Penconi, A. Bossi and D. Ceresoli, *J. Chem. Theory Comput.*, 2020, 1188–1199.
- 56 A. Prlj, B. F. E. Curchod, A. Fabrizio, L. Floryan and C. C. Corminboeuf, *J. Phys. Chem. Lett.*, 2015, **6**, 22.
- 57 R. A. F. Tomas, J. C. M. Bordado, J. F. P. Gomes and R. J. Sheehan, in *Ullmann's Encyclopedia of Industrial Chemistry*, Wiley-VCH Verlag GmbH & Co. KGaA., 2024.
- 58 R. A. F. Tomás, J. C. M. Bordado and J. F. P. Gomes, *Chem. Rev.*, 2013, **113**, 7421–7469.
- 59 N. Aqilah, M. Fadzil, M. Hasbi, A. Rahim and G. P. Maniam, *Chin. J. Catal.*, 2014, **35**, 1641–1652.
- 60 H. M. Lapa and L. M. D. R. S. Martins, *Molecules*, 2023, **28**, art. 1922.
- 61 T. Newhouse and P. S. Baran, *Angew. Chem., Int. Ed.*, 2011, **50**, 3362–3374.
- 62 Y. Yang, G. A. Volpato, E. Rossin, N. Peruffo, F. Tumbarello, C. Nicoletti, R. Bonetto, L. Paoloni, P. Umari, E. Colusso, L. Dell'Amico, S. Berardi, E. Collini, S. Caramori, S. Agnoli and A. Sartorel, *ChemSusChem*, 2023, e202201980.
- 63 R. G. Agarwal, S. C. Coste, B. D. Groff, A. M. Heuer, H. Noh, G. A. Parada, C. F. Wise, E. M. Nichols, J. J. Warren and J. M. Mayer, *Chem. Rev.*, 2022, **122**, 1–49.
- 64 M. Galeotti, M. Salamone and M. Bietti, *Chem. Soc. Rev.*, 2022, **51**, 2171–2223.
- 65 M. Salamone, M. Galeotti, E. Romero-Montalvo, J. A. Van Santen, B. D. Groff, J. M. Mayer, G. A. Dilabio and M. Bietti, *J. Am. Chem. Soc.*, 2021, **143**, 11759–11776.
- 66 N. Holmberg-Douglas and D. A. Nicewicz, *Chem. Rev.*, 2022, **122**, 1925–2016.
- 67 F. Yuan, P. Cao, W. Sun and L. Zhao, *Ind. Eng. Chem. Res.*, 2024, **63**, 82028–8215.
- 68 Z. Li, Y. Dong, Y. Zeng, M. Zhang, H. Lv and G. Y. Yang, *Chin. J. Catal.*, 2024, **66**, 282–291.
- 69 X. Sun, Z. Feng, S. Wang, Q. N. Wang, P. Zhang, R. Li and C. Li, *ACS Catal.*, 2024, **14**, 5356–5365.
- 70 D. Jiang, Q. Zhang, L. Yang, Y. Deng, B. Yang, Y. Liu and C. Zhang, *Renew. Energy*, 2021, **174**, 928–938.
- 71 S. M. Treacy and T. Rovis, *J. Am. Chem. Soc.*, 2021, **143**, 2729–2735.
- 72 Q. Yang, Y. Wang, Y. Qiao, M. Gau, P. J. Carroll, P. J. Walsh and E. J. Schelter, *Science*, 2021, **372**, 847–852.
- 73 E. Skolia, O. G. Mountanea and C. G. Kokotos, *ChemSusChem*, 2024, e202400174.
- 74 S. Rohe, A. O. Morris, T. McCallum and L. Barriault, *Angew. Chem., Int. Ed.*, 2018, **57**, 15664–15669.
- 75 B. Saxena, R. I. Patel and A. Sharma, *RSC Sustain.*, 2024, **2**, 2169–2189.
- 76 Y. Yang, M. Nalesso, A. Basagni, R. Bonetto, R. Signorini, S. Agnoli, L. Đorđević and A. Sartorel, *J. Mater. Chem. A*, 2025, **13**, 18436–18444.



- 77 H. Zhao, J. Joseph, H. Zhang, H. Karoui and B. Kalyanaraman, *Free Radic. Biol. Med.*, 2001, **31**, 599–606.
- 78 S. S. Ranade, D. F. Zamudio Díaz, M. C. Meinke and S. B. Lohan, *Chem. Biol. Interact.*, 2025, **421**, 111744.
- 79 L. Gerritz, J. Wei, T. Fang, C. Wong, A. L. Klodt, S. A. Nizkorodov and M. Shiraiwa, *Environ. Sci. Technol.*, 2024, **58**, 4716–4726.
- 80 M. Trose, M. Dell'Acqua, T. Pedrazzini, V. Pirovano, E. Gallo, E. Rossi, A. Caselli and G. Abbiati, *J. Org. Chem.*, 2014, **79**, 7311–7320.
- 81 J. S. Haynes, J. R. Sams and R. C. Thompson, *Can. J. Chem.*, 1981, **59**, 647–758.
- 82 *CrysAlis PRO*, CrysAlisPRO, Oxford Diffraction /Agilent Technologies UK Ltd, Yarnton, England, 2019.
- 83 G. Sheldrick, *Acta Crystallogr. Sect. A*, 2015, **71**, 3–8.
- 84 L. J. Farrugia, *J. Appl. Crystallogr.*, 2012, **45**, 849–854.
- 85 M. Swart, A. R. Groenhof, A. W. Ehlers and K. Lammertsma, *J. Phys. Chem. A*, 2004, 5479–5483.
- 86 M. Swart, A. W. Ehlers and K. Lammertsma, *Mol. Phys.*, 2004, **102**, 2467–2474.
- 87 A. V Marenich, C. J. Cramer and D. G. Truhlar, *J. Phys. Chem. B*, 2009, **113**, 6378–6396.
- 88 M. M. Flores-Leonar, R. Moreno-Esparza, V. M. Ugalde-Saldívar and C. Amador-Bedolla, *ChemistrySelect*, 2017, **2**, 4717–4724.
- 89 E. A. Bleda, C. Trindle and Z. Altun, *Comput. Theor Chem*, 2015, **1073**, 139–148.
- 90 O. S. Siig and K. P. Kepp, *J. Phys. Chem. A*, 2018, **122**, 4208–4217.
- 91 G. Brauer, *Handbook of preparative inorganic chemistry volume 1, second edition*, Academic press, 1963.
- 92 M. Nardelli, *J. Appl. Cryst.*, 1995, **28**, 659–659.
- 93 B. Bosnich, C. K. Poon and M. L. Tobe, *Inorg. Chem.*, 1965, **4**, 1102–1108.
- 94 R. Ketkaew, Y. Tantirungrotechai, P. Harding, G. Chastanet, P. Guionneau, M. Marchivie and D. J. Harding, *Dalton Trans.*, 2021, **50**, 1086–1096.
- 95 J. M. Holland, J. A. Mcallister, Z. Lu, C. A. Kilner, M. Thornton-Pett and M. A. Halcrow, *Chem. Commun.*, 2001, 577–578.
- 96 J. Elhaik, C. A. Kilner and M. A. Halcrow, *Cryst. Eng. Comm.*, 2005, **7**, 151–157.

View Article Online
DOI: 10.1039/D5DT02534F



The data supporting the article have been included as part of the Supplementary Information. [View Article Online](#)
DOI: 10.1039/D5DT02534F

